PNAS RESEARCH ARTICLE | BIOPHYSICS AND COMPUTATIONAL BIOLOGY

Hydroxo-bridged active site of flavodiiron NO reductase revealed by NRVS and DFT

Filipe Folgosa[a,1], Vladimir Pelmenschikov[b,1,2], Giorgio Caserta[b,1], Matthias Keck[c], Christian Lorent[b], Konstantin Laun[b], Yoshitaka Yoda[d], Leland B. Gee[e], Martin Kaupp[b], Kenji Tamasaku[d], James A. Birrell[f], Ilya Sergueev[g], Christian Limberg[c], Miguel Teixeira[a,2], and Lars Lauterbach[h,2]

Affiliations are included on p. 7.

Edited by Marcetta Darensbourg, Texas A&M University-College Station, College Station, TX; received July 10, 2025; accepted November 20, 2025

The use of oxygen and nitrate as terminal electron acceptors provides organisms with a huge amount of available energy but necessitates methods to detoxify reactive intermediates. The mechanisms of NO and O_2 detoxification in many organisms involve flavodiiron proteins (FDPs). Although the proteinaceous ligands that coordinate the diiron active site of these enzymes are well established, its exact coordination environment remains under debate due to conflicting interpretations of crystallographic and spectroscopic/theoretical studies. Using ^{57}Fe nuclear resonance vibrational spectroscopy (NRVS), complemented by Mössbauer spectroscopy and density functional theory, we elucidated the redox-linked structural changes in the FDP from *Escherichia coli*. The as-isolated diferric state is best described as a dihydroxo-bridged Fe(III)–$(\mu OH^-)_2$–Fe(III) core, which upon reduction converts to a monohydroxo Fe(II)–(μOH^-)–Fe(II) center through the loss of one bridging ligand. This ligand rearrangement defines the structural basis for redox-linked reactivity in FDPs. The study further demonstrates that photoreduction of a stable metalloprotein species can occur under NRVS conditions, indicating that synchrotron-based vibrational measurements may induce subtle redox changes even under low photon flux. These findings provide a mechanistic framework for interpreting redox-linked ligand dynamics in diiron enzymes and highlight the need to collect damage-free X-ray crystal structures avoiding potential beam-induced reduction. Furthermore, diiron active sites are found in numerous other enzyme classes (e.g., methane monooxygenase), and therefore, our findings have implications way beyond the FDPs.

diiron enzymes | NO reduction | reaction mechanism | DFT | NRVS

Significance

Flavodiiron proteins (FDPs) protect cells from nitric oxide (NO) toxicity by converting NO to harmless nitrous oxide (N_2O) at a diiron active site. Despite extensive crystallographic and spectroscopic studies, the detailed structure and redox behavior of this site remained unresolved. Using advanced vibrational spectroscopy and quantum chemical calculations, we reveal how the diiron center rearranges between oxidized and reduced states, releasing a hydroxo bridge undetected by previous X-ray studies. We further show that even weak synchrotron radiation can alter the redox state of metalloproteins, highlighting the need for radiation-damage-free data collection. These insights refine the molecular mechanism of NO detoxification and illustrate general principles governing redox-linked structural dynamics in metalloenzymes.

Nitric oxide (NO) inhibits multiple cellular processes including aerobic respiration and energy metabolism (1). Therefore, NO is produced in response to pathogens by the human innate immune system. To mitigate this threat, microbes utilize dedicated enzymes to detoxify NO. Among these are the flavodiiron proteins (FDPs), which reduce it to innocuous nitrous oxide (N_2O) with water as sole side product (2, 3). FDPs have a minimal core constituted by a metallo-β-lactamase-like domain, containing the catalytic diiron center, and a flavodoxin-like domain with a flavin mononucleotide (FMN). FDP from *Escherichia coli* (*Ec*FDP) contains an extra rubredoxin-like domain located at its C-terminus, which acts as the electron entry point (3, 4), and therefore is also designated as flavorubredoxin. Although some FDPs are able to reduce both dioxygen (O_2) and NO to H_2O and N_2O, respectively, most of them cannot accomplish the two reactions at the same rate, thereby showing preference for one substrate, usually O_2 (5). *Ec*FDP is the only known FDP enzyme with a clear bias toward NO, exhibiting a rate ca. 10 times higher for NO reduction than for O_2 reduction (3). Electrons for this reaction are supplied by NADH via an NADH:flavorubredoxin oxidoreductase (5, 6).

Several X-ray structures of FDPs have been reported, which indicated [with the exception of *Desulfovibrio gigas* FDP (7)] that the active site in the diferric state is coordinated by four histidines, two aspartates, one glutamate, and a nonproteinaceous bridging (μ-)hydroxo ligand (Fig. 1) (8–10). With two histidines and a monodentate glutamate/aspartate at each Fe ion and one bridging aspartate (Asp166 in *Ec*FDP), the metal–ligand core bears an approximate reflection symmetry (Fig. 1). Similar diiron centers, but with distinct coordinating ligands and in a distinct protein scaffold, are found, for example, in the soluble methane monooxygenase (sMMO), whose active site structure is also highly debated (11–13), Δ9-desaturase, R2 ribonucleotide reductase (RNR), (bacterio)ferritin, toluene monooxygenase, hemerythrin, and rubrerythrin (14).

Among the most studied FDP enzymes, we find the O_2-biased protein from *Thermotoga maritima* (*Tm*FDP), whose precise diiron site coordination and catalytic mechanism have

This article is a PNAS Direct Submission.

[1]F.F., V.P., and G.C. contributed equally to this work.

[2]To whom correspondence may be addressed. Email: pelmentschikov@tu-berlin.de, miguel@itqb.unl.pt, or lars.lauterbach@iamb.rwth-aachen.de.

This article contains supporting information online at https://www.pnas.org/lookup/suppl/doi:10.1073/pnas.2512429123/-/DCSupplemental.

Published January 6, 2026.

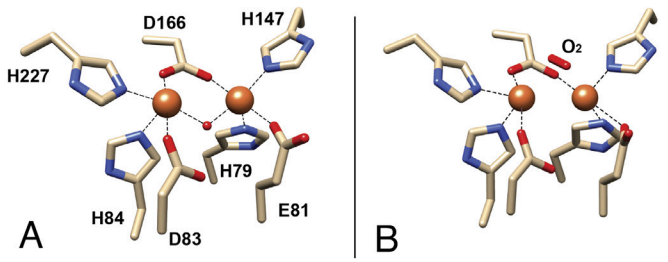

Fig. 1. The active site of *E. coli* FDP as revealed by X-ray crystallography. (*A*) Structure of the as-isolated (oxidized) form (PDB 4D02, 1.75 Å resolution) (8). (*B*) Structure of the sodium dithionite-reduced FDP (PDB 5LLD, 2.65 Å resolution) (8). Orange spheres represent iron ions, while the protein residues are shown with a stick representation. The structure in A shows a μ-hydroxo (μOH^-) ligand bridging the two iron sites, while the structure in *B* contains an O_2 molecule in vicinity of the diiron center (8). A phosphate ion cocrystallized in the as-isolated enzyme structure (*SI Appendix*, Fig. S5) was omitted for clarity.

been the subject of extensive debate (15, 16). X-ray crystallographic data are limited for this FDP (see PDB entry 1VME), however, EPR, Mössbauer spectroscopy, and computational studies have suggested that the diferric state likely adopts a dihydroxo-bridged core, while the diferrous state features a monohydroxo bridge. NO reduction is proposed to proceed with the bridging hydroxo retained throughout the catalytic cycle, with NO binding exclusively to the diferrous site (17–19). In particular, a computational study by Blomberg *et al.* suggested that NO binds directly to the diferrous center, which retains a bridging hydroxo, following dissociation of a water molecule (17). In contrast, a recent MCD (magnetic circular dichroism) study from the Solomon group challenges the presence of a hydroxo bridge between the irons in *Tm*FDP, highlighting persistent uncertainties regarding the diiron coordination and redox-linked ligand arrangements (20).

The active site of *Ec*FDP exhibits unusual features: In the diferrous state, the X-ray structure appears to be devoid of bridging hydroxo ligands, while the as isolated state contains a single hydroxo ligand, in contrast to other FDP structures such as that from *Moorella thermoacetica* (8), where the reduced and oxidized structures both contain a single hydroxo ligand. Instead, for *Ec*FDP, an O_2 molecule was modeled in the diferrous state with a reported Fe···O distance of ~2.6 Å, far longer than typical Fe–O bond lengths (8). Given the relatively low resolution (~2.7 Å) of the diferrous structure and the potential for photodamage during X-ray data collection, it is plausible that the bridging hydroxo escaped detection. To directly probe the *Ec*FDP active site in both the diferric and diferrous states, we employed ^{57}Fe nuclear resonance vibrational spectroscopy (NRVS) in combination with density functional theory (DFT) and Mössbauer spectroscopy. NRVS, a synchrotron-based technique, selectively observes vibrational modes of Mössbauer-active nuclei such as ^{57}Fe (21, 22), and has previously provided detailed structural information on diverse Fe-containing enzymes including hydrogenases (23–25), nitrogenases (26, 27), heme enzymes (28), and nonheme enzymes such as MMOs and dioxygenases (12, 29). Here, we report the vibrational fingerprint of the *Ec*FDP diiron center in both oxidized and reduced states, directly observing different bridging hydroxo species in each redox form. In addition, prolonged NRVS measurements revealed beam-induced modifications at the diiron site, highlighting photoreduction events that must be considered when analyzing both NRVS and X-ray data. Importantly, this study provides direct and internally consistent characterization of the FDP diiron active site, integrating structural, spectroscopic, and computational evidence on the same analogue. This unified approach resolves previous ambiguities regarding the coordination environment and redox-linked ligand rearrangements (20, 30), definitively establishing the presence and role of bridging hydroxo species in both oxidation states.

Results and Discussion

To exclude spectroscopic contributions from the iron of the rubredoxin domain of *Ec*FDP, a truncated form lacking the C-terminus, i.e., having only the two core domains (1 to 400 residues) was used, hereafter referred to as FDP-D. Characterized by comparable spectroscopic and biochemical properties to native *Ec*FDP (6), FDP-D was isolated from a medium enriched with ^{57}Fe. Further details on the sample preparation are described in the *Materials and Methods* section.

Oxidized FDP-D (FDP-D_{OX}). The redox state of as-isolated FDP-D was substantiated by zero-field Mössbauer spectroscopy. The Mössbauer spectrum of FDP-D_{OX} at 13 K (*SI Appendix*, Figs. S1 and S2) is similar to that reported for *Tm*FDP in the oxidized state (16, 30). The isomer shifts of δ = 0.50 and 0.49 mm/s and quadrupole splittings of ΔE_Q = 0.71 and 1.00 mm/s (*SI Appendix*, Tables S1 and S2) of FDP-D_{OX} indicate that both unequal iron centers are high-spin Fe^{3+} in the oxidized as-isolated state. The lack of hyperfine splitting (at zero magnetic field) at this temperature is consistent with an antiferromagnetic coupling of the two Fe spin centers in the presence of at least one bridging ligand as suggested for other FDPs (30).

To examine the coordination of the FDP-D active site irons, vibrational spectroscopy was employed. Initial resonance Raman (RR) spectroscopic experiments on FDP-D_{OX} lacked resonance-enhanced metal–ligand vibrations (31, 32) and produced only signals inherent to the protein-bound FMN prosthetic group (*SI Appendix*, Fig. S3).

FDP-D_{OX}: NRVS and DFT. In contrast to the selection rule limitations of RR spectroscopy (33), ^{57}Fe-NRVS detects exclusively contributions from ^{57}Fe nuclei motion to vibrational modes, thus having high specificity and sensitivity to iron cofactors (25, 34). The ^{57}Fe partial vibrational density of states (^{57}Fe-PVDOS) afforded by NRVS provides a strong handle to validate DFT-calculated geometric and electronic structures of Fe-containing metallocofactors (25, 34, 35). NRVS data on FDP-D_{OX} showed significant changes during its collection time (up to ca. 20 h, *SI Appendix*, Fig. S4*A*). Mössbauer data revealed that a prolonged exposure of FDP-D_{OX} to the 14.4 keV radiation during NRVS measurements resulted in a partial photoreduction of the diiron center (see below). Thus, only the first 4 h of NRVS data of four different samples were used for the representative analysis (Fig. 2*A*). The averaged NRVS spectrum of FDP-D_{OX} displays three major intensity bands at 206, 239, and 269 cm^{-1}. Broader features of decreasing intensity are observed in the 300 to 600 cm^{-1} region. Previous NRVS and DFT studies on a series of high-spin Fe(III)Fe(III) synthetic compounds showed that largely Fe–O/N core vibrational modes contributed to the spectral region between 200 and 300 cm^{-1}, while Fe–O stretches of monooxo, peroxo, and dioxo/hydroxo bridging ligands were identified between 350 and 600 cm^{-1} (36). Remarkably, major NRVS bands of FDP-D_{OX} resemble those recorded for di-oxo/hydroxo compounds [see figure 3 in Park et al. (36)].

Various DFT models of the *Ec*FDP active site were computationally explored. All the models contained invariantly the seven side chains coordinating the two Fe ions as described in the *Materials and Methods* section. The structural alternatives involved modifications of the bridging oxygenous ligands, their

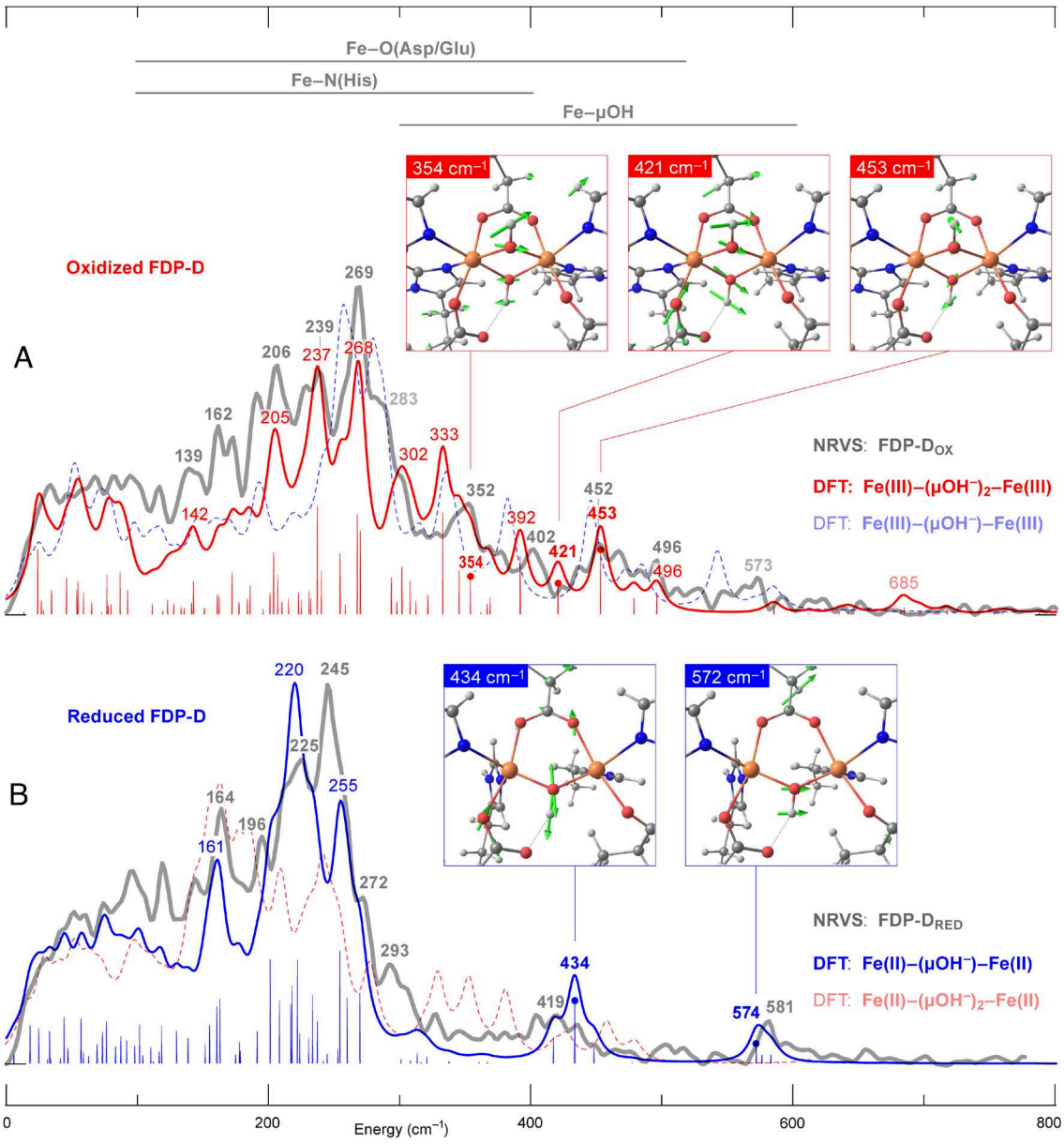

Fig. 2. ^{57}Fe-PVDOS spectra of FDP-D in its (*A*) oxidized and (*B*) reduced states from NRVS experiments (thick gray traces) and DFT calculations (red and blue traces, respectively) using models schematically shown in Fig. 3. Principal Fe-ligand vibrational characters contributing to the spectra are shown on the *Top*. FDP-D sample for the NRVS spectrum in (*B*) was reduced with sodium dithionite; NRVS spectra of NADH-reduced FDP-D samples are shown in *SI Appendix*, Fig. S4 and Fig. 4. Stick-style spectra indicate DFT-calculated normal mode positions and their ^{57}Fe-PVDOS intensities, see alternatively *SI Appendix*, Fig. S22. Selected Fe–μOH$^-$ normal modes are marked with dots and depicted using green arrows. These and other normal mode animations are available as part of the Data and Materials. (37) Full-size DFT models are shown in *SI Appendix*, Figs. S6 and S7. Dashed thin traces display spectra from DFT models with interchanged number of Fe-bridging hydroxo ligands, see alternatively *SI Appendix*, Fig. S15. NRVS spectra including error bars are shown in *SI Appendix*, Figs. S4*A* and S28.

number, and protonation level, including primarily bridging hydroxo OH^- species. Following the X-ray structural data (*SI Appendix*, Fig. S5) (8, 9), weak coordination of either H_2O or O_2 molecules to the *Ec*FDP active site pocket has been further addressed. Possible effects from either the phosphate anion coordination or the vacant bridging site, as resolved in the active sites of as-isolated (oxidized) (PDB 4D02) or dithionite reduced (PDB 5LLD) *Ec*FDP (8), were also investigated. The calculations additionally considered alternatives in the electronic structure and modeling aspects of the protein strain. All these systems are described in *SI Appendix*, *Supplementary DFT Results (SI-DFT)* and listed in *SI Appendix*, Table S4, with their structures and calculated ^{57}Fe-PVDOS spectra displayed correspondingly in *SI Appendix*, Figs. S6–S21.

The best correspondence between the experimental and calculated ^{57}Fe-PVDOS signatures (Fig. 2*A* and *SI Appendix*, Fig. S22*B*) for the FDP-D$_{OX}$ state was produced by a configuration described as Fe(III)–(μOH$^-$)$_2$–Fe(III), as suggested previously for the O_2-biased *Tm*FDP (30). This model retains pseudoreflection symmetry of the metal–ligand core (Figs. 2 and 3 and *SI Appendix*, Figs. S6 and S7), where the mirror plane passes between the two hexacoordinated Fe(III) ions, and encompasses two μOH$^-$ ligands. DFT optimization further suggests an arrangement of the *Ec*FDP active site where the four iron-imidazole Fe(III)–N(His) bonds are coplanar with the diiron-dihydroxo core (Fig. 3). The Fe(III)–(μOH$^-$)$_2$–Fe(III) model matches the observed pattern of FDP-D$_{OX}$ bands in the ~200 to 300 cm^{-1} region, including the global NRVS/DFT maximum at 269/268 cm^{-1}. These bands represent Fe–His/

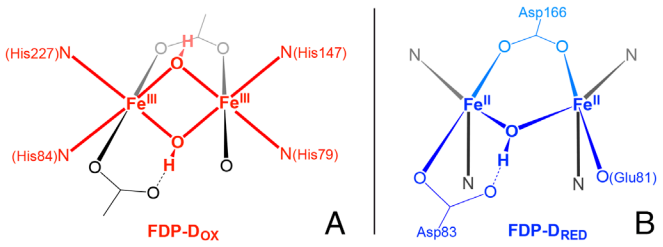

Fig. 3. Proposed metal–ligand arrangements of the diiron core of *Ec*FDP in the two oxidation states (*A*) FDP-D_{OX} and (*B*) FDP-D_{RED}; approximately coplanar ligands are shown correspondingly in red and blue. The active site topology is based on the NRVS-representative DFT models Fe(III)–$(\mu OH^-)_2$–Fe(III) and Fe(II)–(μOH^-)–Fe(II).

Asp/Glu stretches and bends, involving the entire imidazole and carboxylate groups. The DFT model further disclosed a number of mixed Fe–μOH^-/O(Asp,Glu) vibrations in the ~300 to 400 cm^{-1} region, all contributing to the ^{57}Fe-PVDOS. At higher energies, a matching NRVS/DFT band at 452/453 cm^{-1} revealed the underlying normal mode of mostly symmetric Fe–μOH^- (or in-plane, as defined above) stretching character, where the two μOH^- ligands displace in-phase (Fig. 2 *A*, *Right*). The antisymmetric Fe–μOH^- (out-of-plane) modes of FDP-D_{OX} are predicted at lower energies, 421 (in-phase) and 354 (out-of-phase) cm^{-1}, where they couple with the Fe–O(Asp,Glu)/N(His) vibrations gaining higher ^{57}Fe-PVDOS intensities relatively to the isolated Fe–μOH^- motions. Unlike other spectral regions influenced by the protein environment and secondary vibrations, the Fe–OH stretching modes are well isolated and exhibit strong Fe-motion character, making them reliable markers for identifying the Fe(III)–$(\mu OH^-)_2$–Fe(III) structure. Furthermore, mixed Fe–μO–H bending modes were calculated in the ~600 to 800 cm^{-1} spectral region with their ^{57}Fe-PVDOS intensities nearly at (or even below) the experimental noise level (*SI Appendix*, Fig. S22*B*). The mode characters listed above can be traced in the ^{57}Fe–μOH^-/O(Asp,Glu)/N(His) kinetic energy distribution (KED) profiles shown in *SI Appendix*, Fig. S23, as well as in the DFT-based normal mode animations provided as part of the Data and Materials (37). Overall, both the experiment and theory produced ^{57}Fe-PVDOS intensity profiles gradually decline up to ~500 to 600 cm^{-1}.

In line with a known enhanced sensitivity of NRVS features at higher energies (38–40), the bands predicted above 400 cm^{-1} displayed some variability depending on the finer details of the computational models. In particular, the inclusion of a weakly bound water molecule [SI-DFT (*g*), *SI Appendix*, Fig. S13] or modifications to the amino acid restraint scheme using a rigid ("[R]") protein backbone [SI-DFT (*h*), *SI Appendix*, Fig. S14] produced band shifts of up to ~50 cm^{-1} (*SI Appendix*, Figs. S20 and S21). Both cases illustrate enzyme–environment interactions that may not be fully captured by the models. Moreover, experimental factors such as cryogenic heterogeneities [e.g., local pH shifts (41), transient photoreduction, or temperature-dependent structural alterations (40, 42, 43)] could also contribute to discrepancies between experimental and calculated ^{57}Fe-PVDOS features, particularly in the low-energy region. Focusing on the Fe–OH stretching bands thus provides the most robust and interpretable correlation between vibrational signatures and the structural rearrangements occurring at the diiron site.

Reduced FDP-D (FDP-D_{RED}). FDP-D was reduced anaerobically with a sodium dithionite solution (*SI Appendix*) and the redox change was confirmed by zero field Mössbauer spectroscopy. The Mössbauer spectrum of FDP-D_{RED} (*SI Appendix*, Figs. S1, S24, and S25) is similar to that previously reported for reduced *Tm*FDP (30). The isomer shifts of δ = 1.18 and 1.20 mm/s together with quadrupole splittings of ΔE_Q = 2.14 and 2.46 mm/s (*SI Appendix*, Table S1) indicate that both unequal iron species are high-spin Fe(II), confirming reduction of the active site. These two species presumably reflect pentacoordinated iron centers with a vacant coordination site for the NO binding (19, 30), and this agrees with the large values of ΔE_Q, which reflects an anisotropic electric field gradient. Furthermore, the Mössbauer spectrum also shows a third minor feature (12%) characterized by higher isomer shift and quadrupole splitting parameters, tentatively attributed to a hexacoordinated Fe(II) species, originating either from changes in the amino acid(s) coordination or aqueous Fe(II) (44).

FDP-D_{RED}: NRVS and DFT. The NRVS spectrum of FDP-D_{RED} is shown in Fig. 2*B* and *SI Appendix*, Fig. S22*A*. The sodium dithionite reduction produces a shift of the intense bands below 350 cm^{-1} to lower energies, consistent with the diiron center reduction, which results in longer metal–ligand bond lengths (34). The FDP-D_{RED} spectrum shows intense features at 164, 225, and 245 cm^{-1}. At higher energies, a broad 400 to 450 cm^{-1} feature centered at 419 cm^{-1} is observed, as well as a distinct band at 581 cm^{-1}. Notably, the 400 to 450 cm^{-1} feature appears better resolved in a sample reduced in the presence of *E. coli* NADH:flavorubredoxin oxidoreductase, *E. coli* FDP-rubredoxin domain and NADH as the primary reductant (from now on designated as NADH-reduced for simplification) (*SI Appendix*, Fig. S4*B*).

For the diferrous center of FDP-D_{RED}, various Fe(II)Fe(II) DFT models were examined including none, one, or two bridging OH^- ligands, along with other alternatives [SI-DFT (*a-h*)]. For example, the model Fe(II)–$(\mu OH^-)_2$–Fe(II) with two hydroxo ligands (*SI Appendix*, Fig. S8) lacks the distinct 581 cm^{-1} band observed in FDP-D_{RED}, contains too high intensity bands in the ~300 to 400 cm^{-1} region, and shows that the global maximum shifted to 160 cm^{-1} (Fig. 2*B* and *SI Appendix*, Fig. S15*A*). The best fit between the NRVS-observed and DFT-calculated ^{57}Fe-PVDOS signatures (Fig. 2*B* and *SI Appendix*, Fig. S22*A*) was observed using a model with a single hydroxo bridge. This result contrasts with the X-ray structure of the reduced *Ec*FDP (PDB 5LLD), where no hydroxo bridge was observed (8). The redox-dependent release of one hydroxo ligand [plausibly via protonation forming a water molecule (45)] leads to structural transformations (Fig. 2 and *SI Appendix*, Figs. S6 and S7) where the four iron-carboxylate Fe(II)–O(Asp, Glu) bonds become approximately coplanar with the reduced Fe(II)–(μOH^-)–Fe(II) core (Fig. 3).

In the high-intensity region below 300 cm^{-1}, three prominent and matching bands in the FDP-D_{RED} NRVS/DFT spectra are those at 245/255, 225/220 (global maximum), and 164/161 cm^{-1}. Similar to FDP-D_{OX} (see above), these intensities represent Fe–His/Asp/Glu stretches and bends, however in FDP-D_{RED} they manifest in sharper and consolidated peaks, and a well-defined cutoff of the high-intensity region at ~300 cm^{-1}.

In brief, major structural changes in the reduced *Ec*FDP active site comprise an elongation of the Fe···Fe distance to 3.53 Å, as compared to the compressed Fe···Fe = 3.06 Å distance in the dihydroxo-bridged Fe(III)–$(\mu OH^-)_2$–Fe(III) center, in agreement with what might be expected based on charge and bonding considerations. Among the *Ec*FDP protein ligands, the four carboxylates move ~0.1 to 0.2 Å further away from the metal sites upon reduction, thereby redistributing the Fe–O(Asp/Glu) vibrations to predominantly lower frequencies. The Fe-imidazolate distances,

in contrast, remain essentially unaffected upon reduction of the diiron core, exhibiting the corresponding Fe–N(His) vibrational pattern within ~100 to 400 cm^{-1}. This reflects the difference in bonding between carboxylates and imidazoles with metals where the former are highly ionic and the latter show a high degree of covalency.

In the region above 300 cm^{-1}, the matching NRVS/DFT ^{57}Fe-PVDOS features of FDP-D_{RED} are at i) ~400 to 440/420 to 450 (with maxima at 419/434) and ii) 581/574 cm^{-1}. DFT rationalizes these bands as i) symmetric and ii) antisymmetric Fe–μOH^- stretching vibrations (Fig. 2*B*), respectively. These ^{57}Fe-PVDOS features i) and ii) are produced by several normal modes each due to the vibrational coupling between μOH^- and carboxylates from the Fe_P bound Asp83 (denoted proximal, "Fe_P", as the iron is closer to the FMN) and the bridging Asp166. These couplings have i) Fe–O(Asp) stretching and ii) Fe–O–C(Asp) bending character. The vibrational energy order of modes type i) and ii) is opposite in FDP-D_{OX} and FDP-D_{RED}, but in both states the type i) symmetric Fe–μOH^- normal modes produce higher individual ^{57}Fe-PVDOS intensities (*SI Appendix*, Fig. S22). The close correspondence between the experimental and computed Fe–μOH^- bands thus strongly supports the presence of a single bridging hydroxo ligand in the reduced Fe(II)–Fe(II) core.

An important structural element, present in both the FDP-D redox states, is a hydrogen bond between the bridging hydroxo (donor) and carboxylate oxygen of Asp83 (acceptor), Figs. 2 and 3. The characteristic μO(H)···O(Asp) distance at ~2.5 to 2.8 Å, typically found in FDP crystal structures (8–10), is in good agreement with the DFT-optimized distance of ~2.7 to 2.8 Å. A local minimum model avoiding the μOH···O(Asp83) hydrogen bond was found unfavorable by 10 kcal/mol (*SI Appendix*, Fig. S9) and produced an inferior match to the FDP-D_{RED} NRVS data [SI-DFT (*b*) and *SI Appendix*, Fig. S16*A*].

Mössbauer and NRVS Data Highlight Photoreduction of FDP-D Samples. Mössbauer spectra recorded on FDP-D_{OX} after 20 h of NRVS data collection revealed two additional iron species with a total of 12% contribution (*SI Appendix*, Fig. S26 and Table S3). The fitted isomer shifts (δ = 1.28 and 1.24 mm/s) and quadrupole splittings (ΔE_Q = 2.03 and 2.70 mm/s) correspond to high-spin Fe(II) species, which suggest partial photoreduction of the diiron site by the incident 14.4 keV γ-rays (see below) during NRVS measurements. Three additional FDP-D_{OX} samples from the same protein batch were investigated by NRVS for 4, 6, and 10 h data collection intervals, respectively, and their Mössbauer spectra were subsequently recorded (*SI Appendix*, Fig. S27). No changes were observed in the spectra within the first 4 h of the NRVS data collection, while Mössbauer data recorded on samples after 10 h of beam exposure highlighted spectral changes attributed to high-spin Fe(II) species. These species reached an intensity of approximately 6% after 10 h of synchrotron data collection, increasing to 12% after *ca* 20 h of data collection (*SI Appendix*, Table S3 and *Supplementary Results and Discussion*). Prolonged beam exposure causes significant changes in the NRVS spectrum of FDP-D_{OX} (*SI Appendix*, Fig. S4*A*, top spectrum). In fact, comparing the experimental data in the first and last 4 h of data acquisition, we noticed alterations of both the high- and low-energy spectral regions. In particular, the likely partially photoreduced FDP-D_{OX} sample (*SI Appendix*, Fig. S4*A*, 17 to 20 h) does not exhibit the clear absorptions of the representative FDP-D_{OX} spectrum at 352, 402, and 452 cm^{-1} all having significant Fe–μOH vibrational character (Fig. 2*A* and *SI Appendix*, Fig. S4*A*, 1 to 4 h), thereby suggesting photoreduction events and/or partial removal of one OH^- bridging ligand.

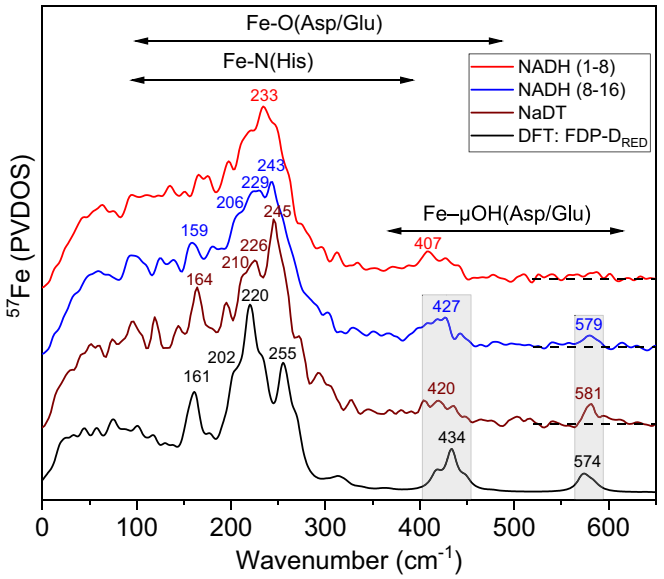

Fig. 4. NRVS characterization of reduced FDP-D. The diiron site was reduced using either its physiological electron transfer partner, NADH:flavorubredoxin oxidoreductase and the *Ec*FDP isolated rubredoxin domain (^{56}Fe, 130 μM) or sodium dithionite. Spectra of NADH-reduced FDP-D were calculated averaging the first 8 h and last 8 h of data collection. Dithionite-reduced FDP-D does not exhibit changes upon prolonged NRVS data collection and is used as a reference to highlight spectral changes in NADH-reduced sample. Major bands are labeled with the corresponding wavenumbers. Color code: DFT data, black; Sodium dithionite reduced FDP-D, brown; NADH-reduced (first 8 h), red; NADH-reduced (last 8 h), blue.

Surprisingly, we also noticed spectral changes in the NRVS spectrum of a NADH-reduced FDP-D sample (Fig. 4, red vs. blue trace). Indeed, comparing the first and the last 8 h of data acquisition, we observed a net increase of the 579 cm^{-1} band, which we assigned to the antisymmetric Fe–μOH^- stretching vibration of the Fe(II)–(μOH^-)–Fe(II) core (Figs. 2*B* and 4). Likely, the NADH- reduction did not result in a completely reduced diiron site, as shown before for *Tm*FDP, which required overnight incubation to become fully reduced (16, 46), and the prolonged exposure of the sample to the 14.41 keV radiation increased the population of the reduced diiron center (Fig. 4, blue trace). The overall spectrum of beam-exposed NADH-reduced FDP-D shows good agreement with the DFT-computed data of FDP-D_{RED} (*SI Appendix*, Fig. S4*B*), further supporting the Fe(III)–$(\mu OH^-)_2$–Fe(III) → Fe(II)–(μOH^-)–Fe(II) transition and reinforcing its mechanistic significance. Some spectral features in the 350 to 500 cm^{-1} energy region show even better correspondence than the sodium dithionite-reduced spectrum, which might indicate possible FDP-D_{RED} alterations by the (nonphysiological) reducing agent (e.g., shifts of NRVS bands associated with protonation/deprotonation events involving protein residues in proximity to the diiron core). It is worth emphasizing that sodium dithionite has been recently shown to be a noninnocent reducing agent when employed to reduce metalloproteins such as hydrogenases (47). Furthermore, no detectable spectral changes have been observed during prolonged data collection on the dithionite-treated FDP-D_{RED} sample, reflecting the retention of a reduced Fe(II)–(μOH^-)–Fe(II) core. Although synchrotron-induced photoreduction of metal centers has been reported in a few cases (12, 48, 52, 53), to the best of our knowledge, prior NRVS observations were limited to highly reactive Fe(IV) = O species in MMO (12), which exist only briefly and rapidly convert into more stable forms. This study, in contrast, provides direct observation of photoreduction in a stable metalloprotein by NRVS. Due to the relatively high

energy of the NRVS X-rays (14.41 keV) but low incident flux (10^9-10^{10} photons s^{-1} mm^{-2}), it was previously postulated that NRVS would not induce noticeable sample damage or alterations over 10 to 20 h accumulation periods.

In conclusion, a comprehensive vibrational characterization of the FDP from *E. coli* addressed its detailed active site composition, geometry, and redox-dependent active site changes. NRVS and DFT identified bands arising from Fe–μOH$^-$ stretching coordinates revealing two bridging hydroxo ligands in the oxidized diferric form of FDP and one bridging hydroxo ligand in the reduced diferrous state (Fig. 3). Other forms of the diiron core coordination explored computationally have been shown to provide an inferior match to the experimental data. These findings shed light on a discrepancy between the diiron coordination found in the available crystallographic data (8), both in the oxidized and reduced forms, as compared with the spectroscopic and computational information gained in this investigation. Accordingly, we speculate that the higher incident fluxes of the X-ray diffraction experiments might have induced photoreduction events resulting in the loss of one hydroxo ligand in the oxidized *Ec*FDP crystallographic structure. We also identified photoreduction of the FDP samples upon prolonged NRVS data collection, which highlights the need of careful evaluation of data obtained using synchrotron radiation. This latter aspect has so far been neglected in the NRVS characterization of Fe-containing metalloproteins.

The proposed structural arrangements for *Ec*FDP have been also drawn for the O_2-biased FDP from *T. maritima*, highlighting conserved redox-dependent changes in the two enzymes (19, 30) where a di-μ-hydroxo diferric site (in the as-isolated enzyme) is reduced to a mono-μ-hydroxo diferrous center. These results yield a clear mechanistic framework for FDPs, explaining prior structural discrepancies and offering broader implications for interpreting metalloenzyme structures obtained under synchrotron irradiation.

Materials and Methods

Sample Preparation. The enzyme construct, FDP-D (residues 1 to 400 of the *norV* gene product, lacking the rubredoxin domain), was produced as previously described (6). To obtain ^{57}Fe enriched samples, the growth medium was supplemented with 0.1 mM $^{57}FeCl_2$ both at the beginning of the growth and at the time of induction. The cells were disrupted by 3 cycles in a French press at 16,000 psi (Thermo) in the presence of DNAse (Applichem) and the crude extract was clarified by low-speed centrifugation at 25,000 g for 25 min and at 138,000 g for 1 h and 30 min and at 4 °C to remove cell debris and the membrane fraction, respectively. The supernatant was dialyzed overnight at 4 °C against 20 mM Tris–HCl, pH 7.5 containing 18% glycerol (buffer A). The soluble extract was then loaded onto a Q-Sepharose Fast-Flow column (50 mL, GE Healthcare) previously equilibrated with buffer A. FDP-D was eluted with a linear gradient from buffer A to 20 mM Tris–HCl, pH 7.5 containing 18% glycerol and 500 mM NaCl. The eluted fractions were analyzed by 15% SDS-PAGE and UV–visible spectroscopy. Fractions containing pure protein were pooled and concentrated. FDP-D sample was quantified and the iron and flavin content was evaluated as previously described (54). The determined Fe/flavin/protein ratio was 2 (±0.2)/0.8 (±0.2)/1. Chemical reduction of FDP-D samples used for NRVS, resonance Raman, and Mössbauer spectroscopy measurements was performed anaerobically, inside a glovebox, by addition of a buffered sodium dithionite solution or with 5 mM NADH together with its physiological electron transfer partner, NADH:flavorubredoxin oxidoreductase and the *Ec*FDP isolated rubredoxin domain (^{56}Fe, 130 μM) (54). Both as prepared and reduced FDP-D samples were 2 mM in protein concentration. The rubredoxin domain of *E. coli* flavorubredoxin and the *E. coli* NADH:flavorubredoxin oxidoreductase were produced and purified as previously described (6).

Mössbauer Spectroscopy. Zero-field Mössbauer spectra were recorded on a SEECO MS6 spectrometer that comprises the following instruments: a JANIS CCS-850 cryostat, including a CTI-CRYOGENICS closed cycle 10 K refrigerator, and a CTI-CRYOGENICS 8200 helium compressor. The cold head and sample mount are equipped with calibrated DT-670-Cu-1.4L silicon diode temperature probes and heaters. The temperature was controlled by a LAKESHORE 335 temperature controller. Spectra were recorded using an LND-45431 Kr gas proportional counter with beryllium window connected to the SEECO W204 γ-ray spectrometer that includes a high voltage supply, a 10 bit and 5 μs ADC and two single channel analyzers. Motor control and recording of spectra was taken care of by the W304 resonant γ-ray spectrometer. For the reported spectra a RITVERC MCO7.114 source (^{57}Co in Rh matrix) with an activity of about 1 GBq was used. All spectra were recorded as frozen solutions at 13 K and data were accumulated for about 24 h. Mössbauer data were processed and fitted using the WMOSS4 program (www.wmoss.org). Isomeric shifts are referenced to α-iron at room temperature.

NRVS. NRVS measurements were performed at SPring-8 BL19LXU and at Petra III P01 (DESY, Germany) with a 0.8–1 meV energy resolution at 14.4125 keV as described previously (25). A 2 × 2 elements avalanche photodiode detector array was used to detect delayed nuclear fluorescence and K fluorescence by ^{57}Fe atoms. All measurements were performed at a 10 to 12 K reading of the cryostat sensor. The real sample temperature, as obtained from the spectral analysis, was 30 to 80 K. The energy scales were calibrated with a $[NEt_4][^{57}FeCl_4]$ sample. To enhance the S/N ratio in the Fe-(OH)x-Fe range of the spectra, sectional measurements of these regions were performed. While for the continuous scans the acquisition time for every point was 5 s, in the sectional scans the acquisition time for every data point was dependent on the region of interest, specifically 20/8/2 s for 400 to 800/300 to 400/–80 to 300 cm^{-1}. For FDP-D_{OX}, the first 4 h of measurements on four independent samples were used for collection of averaged data. The raw NRVS data were analyzed with the PHOENIX software package via the "NRVS Spectra Processing Tool" web interface (https://www.spectra.tools/) to obtain the iron partial vibrational density of states (^{57}Fe-PVDOS) (55-57).

Resonance Raman Spectroscopy. A LabRam HR-800 Jobin Yvon confocal Raman spectrometer coupled to a liquid-N_2-cooled charge-coupled device (CCD) was applied to accumulate resonance Raman spectra of pure FMN (2 mM and 50 mM potassium iodide pH 7.5 in deuterated Tris-HCl 50 mM buffer) and FDP-D samples (pH 7.5 in deuterated Tris-HCl 50 mM buffer). The 458 nm or 514 nm emission lines of an Ar^+ ion laser beam at a power of 1-2 mW was focused on a 2 to 4 μm spot on the surface of the sample drop to induce Raman scattering. The temperature was set to 80 K using a liquid-N_2-cooled cryostage (Linkam Scientific instruments). Toluene was used as an external standard for frequency calibration of each spectrum. Experimental data were analyzed and processed using the Bruker OPUS software version 6.5 or higher.

DFT Calculations. *E. coli* FDP active site topology employed in the present DFT modeling was based on the crystal structure of *Moorella (M.) thermoacetica* FDP in its reduced and subsequently NO-reacted state, which corresponds to an oxidized state (PDB 1YCH) (9). This structure shows a bridging monooxo coordination in the active site. This selection of the X-ray reference based on a protein different from *E. coli* FDP is justified by i) the absence of a cocrystallized species resolved in the active site of *M. thermoacetica* FDP, and ii) otherwise very similar active site arrangements in the two enzymes as shown in *SI Appendix*, Fig. S5. Upon adding protons, the extracted *M. thermoacetica* FDP active site coordinates were conveniently used as a starting structure for the representative FDP-D_{RED} state optimization. The model system involved only the protein side chains binding the Fe sites, terminating at C_α carbons, and saturating them with protons to methyl groups as shown in *SI Appendix*, Fig. S7. At this modeling level, no conflicts are present between the aligned amino acid residues of *E. coli* and *M. thermoacetica* FDPs. The amino acids entering the model are H79(81), E81(83), D83(85), H84(86), H147(148), D166(167), and H227(228), where the protein sequence numbers are for *E. coli* and *M. thermoacetica* FDPs, respectively. All the seven C_α terminal carbon nuclei appearing in the above-described model were locked to their original positions in the X-ray crystallographic structures during structural optimizations (58) and treated as frozen during normal mode analyses. Additionally, an alternative scheme including fixation of the entire $-C_\alpha H_3$ methyl terminals has been investigated, as detailed below in *SI Appendix, Supplementary DFT Results*, subsection (*h*). DFT structure optimizations were done using GAUSSIAN 09 Revision D.01 (59), based on a high-quality initial guess from single point calculations using JAGUAR 9.4 (60). The qualified initial guess approach was specifically employed to ensure broken-symmetry (BS) (61) solutions, with electronic

structures implying open-shell singlet states, unless otherwise mentioned. All the calculations employed the PBE0 (62) hybrid functional in its spin-unrestricted formalism, and the LACV3P** basis set as implemented in JAGUAR 9.4. For the first- and second-row elements, LACV3P** implies 6-311G** triple-ζ basis sets including polarization functions. For the Fe atoms, LACV3P** consists of a triple-ζ basis set for the outermost core and valence orbitals, and the quasi-relativistic Los Alamos effective core potential (ECP) for the innermost electrons. The molecular systems environment was considered using a self-consistent reaction field (SCRF) polarizable continuum model and integral equation formalism (IEF-PCM) (63), with the static dielectric constant set to $\varepsilon = 4.0$ as often used for proteins, and the remaining IEF-PCM parameters at their default values for water. The calculations further included the two-body D3 dispersion corrections by Grimme et al. (64, 65). ^{57}Fe-PVDOS and diatomic internuclear KED spectral intensities were extracted from GAUSSIAN 09 normal mode outputs using an in-house program Q-SPECTOR, successfully applied previously (e.g., in refs. 24, 27, 34, 35, 38-40, and 43). To empirically account for the observed NRVS lineshape, the computed ^{57}Fe-PVDOS and KED intensities were broadened by Lorentzian convolution with a full width at half maximum (FWHM) = 14 cm^{-1}.

Data, Materials, and Software Availability. Data of NRVS and DFT calculations including coordinates of the DFT models and animated normal modes for FDP characterization is available on Zenodo at https://doi.org/10.5281/zenodo.15854815 (37). All other data are included in the manuscript and/or *SI Appendix*.

ACKNOWLEDGMENTS. This work was funded through Fundação para a Ciência e a Tecnologia, Portugal, PTDC/BIA-BQM/0562/2020, MOSTMICRO-ITQB R&D Unit (references UIDB/04612/2020 and UIDP/04612/2020), LS4FUTURE Associated Laboratory (LA/P/0087/2020). This project has also received funding from the European Union's Horizon 2020 research and innovation program under grant agreement No. 810856. We gratefully acknowledge the financial support from the Deutsche Forschungsgemeinschaft under Germany's Excellence Strategy–EXC 2186–390919832–"The Fuel Science Center" and Germany´s Excellence Strategy–EXC 2008–390540038–UniSysCat. J.A.B. acknowledges the Max Planck Society and DFG Priority Programme "Iron-Sulfur for Life: Cooperative Function of Iron-Sulfur Centers in Assembly, Biosynthesis, Catalysis and Disease" (SPP 1927) Project BI 2198/1-1 for funding. We thank Oliver Lenz for generous support by using his laboratories and Peter Hildebrandt, Ingo Zebger, Stephen P. Cramer, and Hongxin Wang for helpful discussions. NRVS experiments at BL19LXU of SPring-8 were approved under proposal no. 2020A1450 and 2016B1316. We acknowledge DESY (Hamburg, Germany), a member of the Helmholtz Association HGF, for the provision of experimental facilities. Parts of this research were carried out at Petra III (photon beamline P01). Beamtime was allocated for proposal I-20210059.

Author affiliations: [a]Instituto de Tecnologia Química e Biológica António Xavier, Universidade Nova de Lisboa, Oeiras 2780-157, Portugal; [b]Institut für Chemie, Technische Universität Berlin, Berlin 10623, Germany; [c]Department of Chemistry, Humboldt-Universität zu Berlin, Berlin 12489, Germany; [d]Precision Spectroscopy Division, SPring-8/JASRI, Sayo 679-5198, Japan; [e]SLAC National Accelerator Laboratory, Menlo Park, CA 94025s; [f]School of Life Science, University of Essex, Colchester CO4 3SQ, United Kingdom; [g]Deutsches Elektronen-Synchrotron, Hamburg 22607, Germany; and [h]Institute of Applied Microbiology, Rheinisch-Westfälische Technische Hochschule (RWTH) Aachen University, Aachen 52074, Germany

Author contributions: V.P., M.T., and L.L. designed research; F.F., V.P., G.C., M. Keck, C. Lorent, K.L., Y.Y., K.T., I.S., and L.L. performed research; F.F., V.P., G.C., L.B.G., M. Kaupp, J.A.B., C. Limberg, M.T., and L.L. analyzed data; and F.F., V.P., G.C., J.A.B., M.T., and L.L. wrote the paper.

The authors declare no competing interest.

1. A. M. Gardner, R. A. Helmick, P. R. Gardner, Flavorubredoxin, an inducible catalyst for nitric oxide reduction and detoxification in *Escherichia coli*. *J. Biol. Chem.* **277**, 8172–8177 (2002).
2. R. Silaghi-Dumitrescu *et al.*, A flavodiiron protein and high molecular weight rubredoxin from *Moorella thermoacetica* with nitric oxide reductase activity. *Biochemistry* **42**, 2806–2815 (2003).
3. C. M. Gomes *et al.*, A novel type of nitric-oxide reductase. *Escherichia coli* flavorubredoxin. *J. Biol. Chem.* **277**, 25273–25276 (2002).
4. F. Folgosa, M. C. Martins, M. Teixeira, Diversity and complexity of flavodiiron NO/O_2 reductases. *FEMS Microbiol. Lett.* **365**, fnx267 (2018).
5. M. C. Martins *et al.*, How superoxide reductases and flavodiiron proteins combat oxidative stress in anaerobes. *Free Radic. Biol. Med.* **140**, 36–60 (2019).
6. J. B. Vicente, M. Teixeira, Redox and spectroscopic properties of the *Escherichia coli* nitric oxide-detoxifying system involving flavorubredoxin and its NADH-oxidizing redox partner. *J. Biol. Chem.* **280**, 34599–34608 (2005).
7. C. Frazao *et al.*, Structure of a dioxygen reduction enzyme from *Desulfovibrio gigas*. *Nat. Struct. Biol.* **7**, 1041–1045 (2000).
8. C. V. Romao *et al.*, Structure of *Escherichia coli* flavodiiron nitric oxide reductase. *J. Mol. Biol.* **428**, 4686–4707 (2016).
9. R. Silaghi-Dumitrescu, D. M. Kurtz Jr., L. G. Ljungdahl, W. N. Lanzilotta, X-ray crystal structures of *Moorella thermoacetica* FprA. Novel diiron site structure and mechanistic insights into a scavenging nitric oxide reductase. *Biochemistry* **44**, 6492–6501 (2005).
10. A. Di Matteo *et al.*, The O_2-scavenging flavodiiron protein in the human parasite *Giardia intestinalis*. *J. Biol. Chem.* **283**, 4061–4068 (2008).
11. D. Kass *et al.*, Spectroscopic properties of a biologically relevant [$Fe_2(\mu$-$O)_2$] diamond core motif with a short iron-iron distance. *Angew. Chem. Int. Ed. Engl.* **62**, e202209437 (2023).
12. A. B. Jacobs *et al.*, Nuclear resonance vibrational spectroscopic definition of the Fe(IV)$_2$ intermediate Q in methane monooxygenase and its reactivity. *J. Am. Chem. Soc.* **143**, 16007–16029 (2021).
13. C. E. Schulz, R. G. Castillo, D. A. Pantazis, S. DeBeer, F. Neese, Structure-spectroscopy correlations for intermediate Q of soluble methane monooxygenase: Insights from QM/MM calculations. *J. Am. Chem. Soc.* **143**, 6560–6577 (2021).
14. A. J. Jasniewski, L. Que Jr., Dioxygen activation by nonheme diiron enzymes: Diverse dioxygen adducts, high-valent intermediates, and related model complexes. *Chem. Rev.* **118**, 2554–2592 (2018).
15. M. R. A. Blomberg, P. Adelroth, Reduction of O_2 and NO in flavodiiron proteins–Tuning the energy landscape by second sphere ligation variations. *J. Inorg. Biochem.* **270**, 112943 (2025).
16. J. D. Caranto, A. Weitz, M. P. Hendrich, D. M. Kurtz Jr., The nitric oxide reductase mechanism of a flavo-diiron protein: Identification of active-site intermediates and products. *J. Am. Chem. Soc.* **136**, 7981–7992 (2014).
17. S. Biswas, D. M. Kurtz, S. R. Montoya, M. P. Hendrich, E. L. Bominaar, The catalytic role of a conserved tyrosine in nitric oxide-reducing non-heme diiron enzymes. *ACS Catal.* **10**, 8177–8186 (2020).
18. J. Lu, B. Bi, W. Lai, H. Chen, Origin of nitric oxide reduction activity in flavo-diiron NO reductase: Key roles of the second coordination sphere. *Angew. Chem. Int. Ed. Engl.* **58**, 3795–3799 (2019).
19. A. C. Weitz *et al.*, Spectroscopy and DFT calculations of flavo-diiron nitric oxide reductase identify bridging structures of NO-coordinated diiron intermediates. *ACS Catal.* **8**, 11704–11715 (2018).
20. W. J. Transue, R. A. Snyder, J. D. Caranto, D. M. Kurtz Jr., E. I. Solomon, Particle swarm fitting of spin hamiltonians: Magnetic circular dichroism of reduced and NO-bound flavodiiron protein. *Inorg. Chem.* **61**, 16520–16527 (2022).
21. W. R. Scheidt, J. Li, J. T. Sage, What can be learned from nuclear resonance vibrational spectroscopy: Vibrational dynamics and hemes. *Chem. Rev.* **117**, 12532–12563 (2017).
22. C. Lorent, G. Caserta, V. Schünemann, I. Zebger, "Vibrational and Mössbauer spectroscopic techniques to study iron–sulfur clusters." in *Iron–Sulfur Clusters*, S. Leimkühler, G. Schwarz, O. Lenz, O. Einsle, Eds. (Wiley-VCH GmbH, 2025) pp. 571–616.
23. G. Caserta *et al.*, Stepwise assembly of the active site of [NiFe]-hydrogenase. *Nat. Chem. Biol.* **19**, 498–506 (2023).
24. E. J. Reijerse *et al.*, Direct observation of an iron-bound terminal hydride in [FeFe]-hydrogenase by nuclear resonance vibrational spectroscopy. *J. Am. Chem. Soc.* **139**, 4306–4309 (2017).
25. L. Lauterbach *et al.*, Nuclear resonance vibrational spectroscopy reveals the FeS cluster composition and active site vibrational properties of an O_2-tolerant NAD$^+$-reducing [NiFe] hydrogenase. *Chem. Sci.* **6**, 1055–1060 (2015).
26. C. Van Stappen *et al.*, Structural correlations of nitrogenase active sites using nuclear resonance vibrational spectroscopy and QM/MM calculations. *Faraday Discuss.* **243**, 253–269 (2023).
27. A. D. Scott *et al.*, Structural characterization of CO-inhibited Mo-nitrogenase by combined application of nuclear resonance vibrational spectroscopy, extended X-ray absorption fine structure, and density functional theory: New insights into the effects of CO binding and the role of the interstitial atom. *J. Am. Chem. Soc.* **136**, 15942–15954 (2014).
28. M. G. Galinato *et al.*, Heme-protein vibrational couplings in cytochrome c provide a dynamic link that connects the heme-iron and the protein surface. *Proc. Natl. Acad. Sci. U.S.A.* 109, 8896–8900 (2012).
29. M. Srnec *et al.*, Nuclear resonance vibrational spectroscopic definition of the facial triad Fe(IV)═O intermediate in taurine dioxygenase: Evaluation of structural contributions to hydrogen atom abstraction. *J. Am. Chem. Soc.* **142**, 18886–18896 (2020).
30. A. C. Weitz *et al.*, Spectroscopy and DFT calculations of a flavo-diiron enzyme implicate new diiron site structures. *J. Am. Chem. Soc.* **139**, 12009–12019 (2017).
31. T. Hayashi, J. D. Caranto, H. Matsumura, D. M. Kurtz Jr., P. Moenne-Loccoz, Vibrational analysis of mononitrosyl complexes in hemerythrin and flavodiiron proteins: Relevance to detoxifying NO reductase. *J. Am. Chem. Soc.* **134**, 6878–6884 (2012).
32. T. Hayashi, J. D. Caranto, D. A. Wampler, D. M. Kurtz, P. Moenne-Loccoz, Insights into the nitric oxide reductase mechanism of flavodiiron proteins from a flavin-free enzyme. *Biochemistry* **49**, 7040–7049 (2010).
33. G. Caserta *et al.*, Unusual structures and unknown roles of FeS clusters in metalloenzymes seen from a resonance Raman spectroscopic perspective. *Coord. Chem. Rev.* **452**, 214287 (2022).
34. L. Lauterbach *et al.*, Characterization of the [3Fe-4S](0/1+) cluster from the D14C variant of *Pyrococcus furiosus* ferredoxin via combined NRVS and DFT analyses. *Dalton Trans.* **45**, 7215–7219 (2016).
35. Y. T. Tseng *et al.*, Substrate-gated transformation of a pre-catalyst into an iron-hydride intermediate [(NO)(2)(CO)Fe(mu-H)Fe(CO)(NO)(2)](-) for catalytic dehydrogenation of dimethylamine borane. *Inorg. Chem.* **62**, 769–781 (2023).
36. K. Park *et al.*, Nuclear resonance vibrational spectroscopic and computational study of high-valent diiron complexes relevant to enzyme intermediates. *Proc. Natl. Acad. Sci. U.S.A.* 110, 6275–6280 (2013).
37. F. Folgosa *et al.*, Dataset for the publication: Hydroxo-bridged active site of flavodiiron NO reductase revealed by NRVS and DFT. Zenodo. https://doi.org/10.5281/zenodo.15854815. Deposited 10 July 2025.
38. L. B. Gee *et al.*, Vibrational characterization of a diiron bridging hydride complex–A model for hydrogen catalysis. *Chem. Sci.* **11**, 5487–5493 (2020).
39. V. Pelmenschikov *et al.*, Reaction coordinate leading to H_2 production in [FeFe]-hydrogenase identified by nuclear resonance vibrational spectroscopy and density functional theory. *J. Am. Chem. Soc.* **139**, 16894–16902 (2017).

40. G. Caserta *et al.*, Hydroxy-bridged resting states of a [NiFe]-hydrogenase unraveled by cryogenic vibrational spectroscopy and DFT computations. *Chem. Sci.* **12**, 2189–2197 (2020).
41. N. A. Sieracki, H. J. Hwang, M. K. Lee, D. K. Garner, Y. Lu, A temperature independent pH (TIP) buffer for biomedical biophysical applications at low temperatures. *Chem. Commun.* **7**, 823–825 (2008).
42. S. T. Stripp, S. Mebs, M. Haumann, Temperature dependence of structural dynamics at the catalytic cofactor of [FeFe]-hydrogenase. *Inorg. Chem.* **59**, 16474–16488 (2020).
43. J. A. Birrell *et al.*, Spectroscopic and computational evidence that [FeFe] hydrogenases operate exclusively with CO-bridged intermediates. *J. Am. Chem. Soc.* **142**, 222–232 (2020).
44. J. B. Gordon *et al.*, Structures, spectroscopic properties, and dioxygen reactivity of 5- and 6-coordinate nonheme iron(II) complexes: A combined enzyme/model study of thiol dioxygenases. *J. Am. Chem. Soc.* **140**, 14807–14822 (2018).
45. M. R. A. Blomberg, P. Ädelroth, Reduction of nitric oxide to nitrous oxide in flavodiiron proteins: Catalytic mechanism and plausible intermediates. *ACS Catal.* **13**, 2025–2038 (2023).
46. K. Karstens *et al.*, Impact of the iron-sulfur cluster proximal to the active site on the catalytic function of an O_2-tolerant NAD^+-reducing [NiFe]-hydrogenase. *Biochemistry* **54**, 389–403 (2015).
47. M. A. Martini *et al.*, The nonphysiological reductant sodium dithionite and [FeFe] hydrogenase: Influence on the enzyme mechanism. *J. Am. Chem. Soc.* **143**, 18159–18171 (2021).
48. C. Kisker *et al.*, Molecular basis of sulfite oxidase deficiency from the structure of sulfite oxidase. *Cell* **91**, 973–983 (1997).
49. G. N. George, I. J. Pickering, C. Kisker, X-ray absorption spectroscopy of chicken sulfite oxidase crystals. *Inorg. Chem.* **38**, 2539–2540 (1999).
50. G. E. Cutsail *et al.*, High-resolution iron X-ray absorption spectroscopic and computational studies of non-heme diiron peroxo intermediates. *J. Inorg. Biochem.* **203**, 110877 (2020).
51. M. D. Clay *et al.*, Spectroscopic studies of *Pyrococcus furiosus* superoxide reductase: Implications for active-site structures and the catalytic mechanism. *J. Am. Chem. Soc.* **124**, 788–805 (2002).
52. K. G. V. Sigfridsson *et al.*, Rapid X-ray photoreduction of dimetal-oxygen cofactors in ribonucleotide reductase. *J. Biol. Chem.* **288**, 9648–9661 (2013).
53. M. C. Corbett *et al.*, Photoreduction of the active site of the metalloprotein putidaredoxin by synchrotron radiation. *Acta Crystallogr. Sect. D Biol. Crystallogr.* **63**, 951–960 (2007).
54. F. Folgosa, M. C. Martins, M. Teixeira, The multidomain flavodiiron protein from *Clostridium difficile* 630 is an NADH:oxygen oxidoreductase. *Sci. Rep.* **8**, 10164, (2018).
55. L. B. Gee, H. Wang, S. P. Cramer, NRVS for Fe in biology: Experiment and basic interpretation. *Methods Enzymol.* **599**, 409–425 (2018).
56. W. Sturhahn, CONUSS and PHOENIX: Evaluation of nuclear resonant scattering data. *Hyperfine Interact.* **125**, 149–172 (2000).
57. L. B. Gee, spectra.tools. https://www.spectra.tools/. Accessed 10 July 2025.
58. V. Pelmenschikov, M. R. Blomberg, P. E. Siegbahn, A theoretical study of the mechanism for peptide hydrolysis by thermolysin. *J. Biol. Inorg. Chem.* **7**, 284–298 (2002).
59. M. J. Frisch *et al.*, *Gaussian 09, Revision D.01* (Gaussian Inc., Wallingford, CT, 2009).
60. A. D. Bochevarov *et al.*, Jaguar: A high-performance quantum chemistry software program with strengths in life and materials sciences. *Int. J. Quantum. Chem.* **113**, 2110–2142 (2013).
61. L. Noodleman, D. A. Case, Density-functional theory of spin polarization and spin coupling in iron-sulfur clusters. *Adv. Inorg. Chem.* **38**, 423–458 (1992).
62. C. Adamo, V. Barone, Toward reliable density functional methods without adjustable parameters: The PBE0 model. *J. Chem. Phys.* **110**, 6158–6170 (1999).
63. J. Tomasi, B. Mennucci, R. Cammi, Quantum mechanical continuum solvation models. *Chem. Rev.* **105**, 2999–3093 (2005).
64. L. Goerigk, S. Grimme, A thorough benchmark of density functional methods for general main group thermochemistry, kinetics, and noncovalent interactions. *Phys. Chem. Chem. Phys.* **13**, 6670–6688 (2011).
65. S. Grimme, J. Antony, S. Ehrlich, H. Krieg, A consistent and accurate ab initio parametrization of density functional dispersion correction (DFT-D) for the 94 elements H-Pu. *J. Chem. Phys.* **132**, 154104 (2010).